Magazine of Civil Engineering

ISSN 2712-8172

journal homepage: http://engstroy.spbstu.ru/

Research article

UDC 624.04

DOI: 10.34910/MCE.111.2

High-strength steel effects on the behavior of special shear walls

H. Arshadi* ✉, ***A. Kheyroddin***, ***A. Asadollahi Nezhad***

Semnan University, Semnan, Iran

✉ *hamed.arshadi@semnan.ac.ir*

Keywords: high-strength steel (HSS), reinforced-concrete (RC) structures, shear wall, finite element analysis (FEA), nonlinear behavior

Abstract. In this research, the effects of applying high-strength steel (HSS) bars as horizontal and vertical bars of the web, and as the flexural and shear bars of the boundary elements on the behavior (load-displacement and maximum moment) of shear walls, were analytically investigated in 45 specimens by finite element analysis (FEA). In addition, the influence of concrete strength along with using HSS bars in the shear walls was studied. The results showed that HSS application as flexural bars of boundary elements improved the performance of shear walls more than other cases of bar locations. However, their shear reinforcement application did not affect their performance significantly. Moreover, HSS usage as the horizontal and vertical bars of the web of the shear walls improved the performance of the specimens. Finally, using higher-strength steel was more effective on the shear performance of shear walls than their moment performance.

1. Introduction

Reinforced-concrete (RC) material is the most popular construction material, because of its financial benefits. The failure mode of RC members is complex with respect to the brittle failure mode of concrete and the ductile failure mode of steel. One of the important issues related to the RC structures is the lateral-resisting systems to endure lateral loads such as wind and earthquake loads. The lateral-resisting systems are generally classified into three categories: shear walls, moment frames, and dual systems [1]. Shear walls are rather the most efficient systems in earthquake-resistant structures. They have several benefits in comparison to the moment frames. They are used either with or without boundary elements. They provide high strength and stiffness, which leads to a decrease in the lateral displacements of the RC structures. Thus, they also limit the P-Δ effects which can be a significant benefit in the tall buildings. However, shear walls can cause uplift forces in the bottom of structures which is a disadvantage. They can be used along with steel or RC moment frames. In this case, they have an interaction with the moment frames and cause negative shear forces at the top of the structures. For this reason, the thickness of the shear walls should gradually be decreased in the higher stories of the structures. Dual systems have two defensive fronts, unlike only the moment frames or shear walls. This issue is a great advantage.

These days, steel bars with an f_y of greater than 500 MPa are considered as HSS bars. The motivation of using HSS bars is their various economic and executive benefits such as decreasing steel consumption, expenses related to their shipment and placement, improving the concrete quality by decreasing the setback of steel congestion in the RC members, and reducing construction time [2].

Arshadi, H., Kheyroddin, A., Asadollahi Nezhad, A. High-strength steel effects on the behavior of special shear walls. Magazine of Civil Engineering. 2022. 111(3). Article No. 11102. DOI: 10.34910/MCE.111.2

However, there are serious obstacles against using HSS bars, such as crack widening under service loads due to increasing stress level of steel bars, brittle failure (where concrete crushing happens before steel yielding), decreasing the stiffness of RC members, and decreasing ductility of RC structures [3]. Thus, HSS use is limited in the seismic areas by building codes, especially in the structural RC members such as shear walls. Some of these limitations are due to a lack of sufficient information and analytical data about HSS influences on the behavior of shear walls. In the 1971 edition of ACI 318, the yield strength of HSS bars was limited to 560 MPa [4]. Also, ACI 318-08 allowed steel bars with a yield strength not exceeding 560 MPa [5]. In Japan, bars with an f_y of 700 MPa are permitted to be applied in the structural elements [6].

The seismic performance of RC structures with HSS bars has been investigated by researchers, lately. Zhou *et al.* (2013) tested a series of RC beams with HSS to investigate the crack widths and displacement of them [7]. The most important technical source about HSS application in structures is a report collected by the NEHRP consultant joint venture [5]. This report reviewed all the published researches about HSS bars all over the world until the time of its production. Kolozvary and Wallace (2016) analytically studied nonlinear modeling of RC shear walls [8]. They utilized numerical models that combined coupled P-M-V behavior in a five-story RC wall-frame building. Kolozvari *et al.* (2018) researched new modeling approaches for simulating nonlinear flexural and coupled shear-flexural behavior of shear walls [9]. Arshadi *et al.* (2019) performed a series of experiments on the special moment frames and beam-column connections (BCCs) subjected to seismic loading [3, 10]. They studied several criteria such as energy absorption, ductility, cracking, etc. They demonstrated that applying HSS bars led to decreases in energy dissipation and ductility of these specimens. Arshadi *et al.* (2020) also experimentally studied several damage indices of RC frames and BCCs with HSS bars [11]. They reported that using HSS bars generally expedited the damage distribution and failure of the specimens.

As discussed in the paragraphs above, despite the various benefits of HSS bars, their application is restricted due to the mentioned challenges, especially in the special shear walls and moment frames [12]. This phenomenon can be due to a lack of experimental and analytical data about the seismic behavior of shear walls with HSS bars. Unfortunately, most of the studies have been focused on using HSS bars in beams or columns and not in the shear walls. Then, the NEHRP report strongly advised studying the HSS effects on the behavior of shear walls [5]. Thus, the effects of HSS bars with the yield strengths of 560 and 700 MPa as horizontal and vertical bars of the web, and also as the flexural and shear bars of the boundary elements on the behavior of shear walls were analytically investigated by finite element analysis (FEA) in this research. The effects of compressive strength of concrete (with the compressive strengths of 30, 45, and 60 MPa) along with the application of HSS bars were studied in the shear walls, too. The results showed that HSS application as flexural bars of boundary elements improved the performance of shear walls. However, their application as the shear bars of them did not affect their performance, conspicuously. Moreover, HSS application as the horizontal and vertical bars of the web of the specimens improved their performance. Also, using higher-strength concrete was less effective than using higher-strength steel on the maximum base shear and the ultimate moment of the specimens. The results showed that applying higher-strength steel was more effective on the shear performance of shear walls than their moment performance.

2. Methods

2.1. Concrete Damage Plasticity (CDP)

There are three different models to simulate the concrete behavior in the FEA software such as smeared crack concrete (SCC) model, brittle cracking (BC) model, and concrete damage plasticity (CDP) model [13]. Every model is suitable for special types of structures and loading situations. However, the most comprehensive model is the CDP model which is a continuous one with damage based on plasticity for concrete. According to the basic presumption of CDP, the major failure mechanisms of RC structures are described by tensile cracking in tension and compressive crushing [14]. In this section, the basic presumptions of CDP modeling are asserted. Equation 1 is used to reach strain decomposition rate, which is assumed for the rate-independent model [14]:

$$\dot{\varepsilon} = \dot{\varepsilon}^{el} + \dot{\varepsilon}^{pl}, \tag{1}$$

$\dot{\varepsilon}$ is the total strain rate, $\dot{\varepsilon}^{el}$ is the elastic portion of strain, and $\dot{\varepsilon}^{pl}$ is the plastic portion of it. With respect to scalar damaged elasticity, the stress-strain relationship is defined as Equation 2:

$$\sigma = (1-d)D_0^{el} : \left(\varepsilon - \varepsilon^{pl}\right) = D^{el} : \left(\varepsilon - \varepsilon^{pl}\right), \tag{2}$$

D_0^{el} is undamaged elastic stiffness of material; $D^{el} = (1-d) D_0^{el}$ is degraded elastic stiffness, and d is scalar stiffness depreciation variable (regarded as zero for undamaged material and as one for the completely damaged one). With regard to the scalar-damage notion, the stiffness depreciation is regarded as isotropic and characterized by d (a single depreciation parameter). Succedent the continuum-damage mechanics, the effective stress is calculated by Equation 3. Moreover, Equation 4 is utilized to compute the Cauchy stress (related to the effective stress by the scalar depreciation formulation):

$$\overline{\sigma}^{def} = D_0^{\theta l} : \left(\varepsilon - \varepsilon^{pl}\right), \tag{3}$$

$$\sigma = (1-d)\overline{\sigma}, \tag{4}$$

$\overline{\varepsilon}_t^{pl}$ and $\overline{\varepsilon}_c^{pl}$ are hardening variables and assigned to regard damage situations in tension and compression. $\overline{\varepsilon}_t^{pl}$ is equivalent plastic tensile strain and $\overline{\varepsilon}_t^{pl}$ is the equivalent plastic compressive strain. Cracking distribution initiates by an increase in the values of hardening parameters. Lubliner *et al.* suggested a model to define the yield surface function which was revised by Lee and Fenves (Fig. 1)[15]. The yield surface function can be computed by Equation 5:

$$F = \frac{1}{1-\alpha}\left(\overline{q} - 3\alpha\overline{p} + \beta\left(\tilde{\varepsilon}^{pl}\right)\left(\overline{\sigma}_{\max} - \gamma\left(\overline{\sigma}_{\max}\right)\right)\right) - \tilde{\sigma}_c\left(\tilde{\varepsilon}_c^{pl}\right) \le 0, \tag{5}$$

$\overline{q}$ is the equivalent Von-Mises stress, $\overline{p}$ is effective hydrostatic pressure, $< x \ge \frac{1}{2}\left(x + |x|\right)$ is the Macauley bracket function; $\overline{\sigma}_{\max}$ is the algebraically maximum eigenvalue of tensor $\overline{\sigma}_c$; α, β and γ are dimensionless constants of materials, calculated by Equations 6, 7, and 8:

$$\alpha = \frac{\left(\sigma_{b0}/\sigma_{c0}\right) - 1}{2\left(\sigma_{b0}/\sigma_{c0}\right) - 1}; \; 0 \le \alpha \le 0.5, \tag{6}$$

$\left(\sigma_{b0}/\sigma_{c0}\right)$ is the ratio of biaxial compressive stress to uniaxial compressive yield one which influences the yield surface in a plane-stress situation. $\left(\sigma_{b0}/\sigma_{c0}\right)$ values for concrete are in the range from 1.10 to 1.16. Then, the α values will be between 0.08 and 0.12.

$$\beta\left(\tilde{\varepsilon}^{pl}\right) = \frac{\overline{\sigma}_c\left(\tilde{\varepsilon}_c^{pl}\right)}{\overline{\sigma}_t\left(\tilde{\varepsilon}_t^{pl}\right)}(1-\alpha) - (1+\alpha), \tag{7}$$

$\overline{\sigma}_c\left(\tilde{\varepsilon}_c^{pl}\right)$ and $\overline{\sigma}_t\left(\tilde{\varepsilon}_t^{pl}\right)$ are the effective cohesion stress in compression and tension, respectively.

$$\gamma = \frac{3(1-k_c)}{2k_c - 1}, \tag{8}$$

The γ coefficient is used only for the triaxial compressive stress state. k_c is the ratio of the hydrostatic effective stress in tensile meridian to that of the compressive meridian when the maximum principal stress is negative. As shown in Fig. 1, this parameter is the coefficient that ascertains the shape of the deviatoric cross-section. According to experimental results, the CDP damage proposes to regard the default value $k_c = 2/3$.

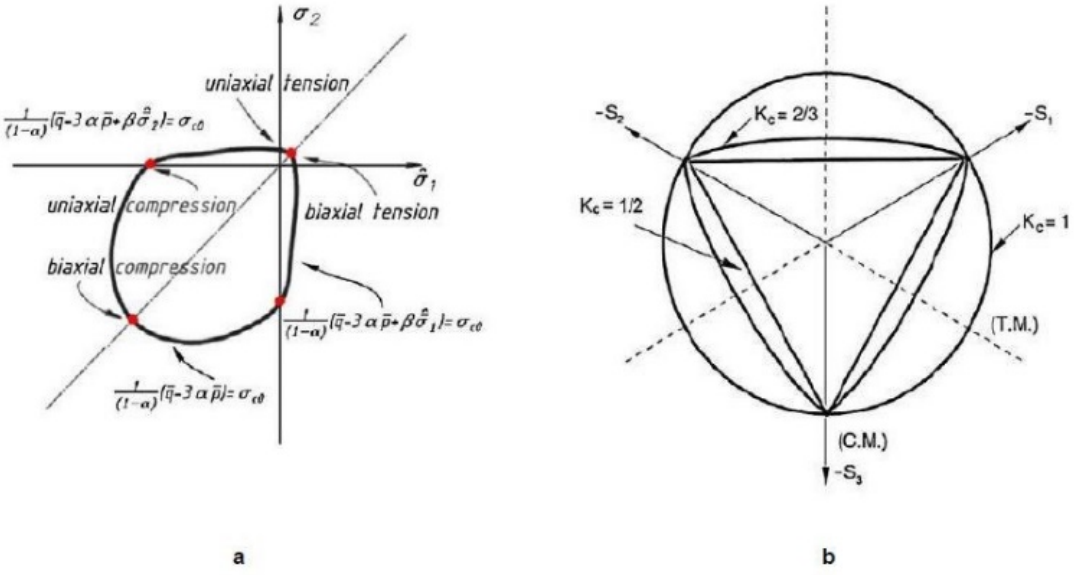

Figure 1. Concrete damage plasticity (CDP) model:
a) yield surface in plane stress, and b) yield surface in the deviatoric plane [15].

The flow rule is utilized to make a relation between the yield surface stress and the stress-strain relationship. The CDP model utilizes Drucker-Prager hyperbolic function as a non-associated flow potential function using Equation 9 [15]:

$$G = \sqrt{\left(\zeta \sigma_{t0} \tan\psi\right)^2 + \overline{q}^2} - \overline{p}\tan\psi, \tag{9}$$

ζ is the potential flow eccentricity that sets the hyperbola shape in plastic potential flow function. ζ is a low positive value that is described as the ratio of concrete tensile strength to its compressive strength, σ_{t0} is uniaxial tensile stress, ψ is dilatation angle. This parameter characterizes concrete performance when it is subjected to a triaxial compound stress state.

2.2. Finite Element Analysis

In this research, a 2-noded truss element (T3D2) with three freedom degrees in each node was used to model bars. 8-noded brick element (C3D8R) with reduced integration and three freedom degrees in each node was used to model concrete. The embedded method with a perfect bond between concrete and steel was assigned to simulate the concrete-reinforcement reaction.

2.2.1 Concrete

As shown in Fig. 2, the stress-strain behavior of concrete was simulated by the Equations 10.a, 10.b, and 10.c:

$$\sigma_{c,1} = E_c \varepsilon_c, \ \varepsilon_c \le \frac{0.4 f_c'}{E_c}; \tag{10a}$$

$$\sigma_{c,2} = \frac{\eta_c \dfrac{\varepsilon_c}{\varepsilon_0} - \left(\dfrac{\varepsilon_c}{\varepsilon_0}\right)^2}{1 + \left(\eta_c - 2\right)\dfrac{\varepsilon_c}{\varepsilon_0}} f_c', \ \frac{0.4 f_c'}{E_c} \le \varepsilon_c \le 0.0035; \tag{10b}$$

$$\sigma_{c,3} = \left(\frac{2 + \lambda_c f_c' \varepsilon_0}{2 f_c'} - \lambda_c \varepsilon_0 + \frac{\lambda_c \varepsilon_c^2}{2\varepsilon_0}\right)^{-1}, 0.0035 \le \varepsilon_c \le 0.03. \tag{10c}$$

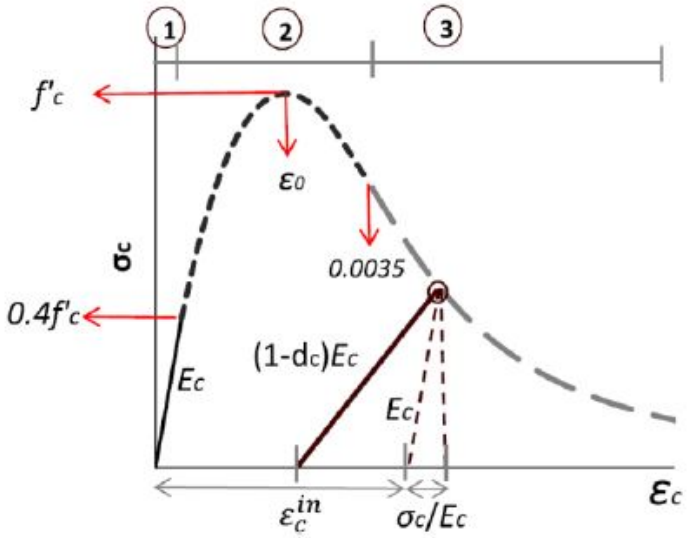

Figure 2. Uniaxial compressive stress-strain diagram for concrete [16].

Equation 10a demonstrates the linear-elastic branch, where ε_c is a variable changes from zero to $0.4 f_c' / E_c$, and E_c is the initial modulus of elasticity. The linear branch ends at the stress level $0.4 f_c'$. Equation 9b defines the second branch up to the strain level of 0.0035 in the descending branch. The corresponding strain level at the peak stress is defined as $\varepsilon_0 = 2 f_c' / E_c$; η_c is material constant. The stress and strain compatibility at the strain level of $\varepsilon_c = 0.4 f_c' / E_c$, Equations (10a) and (10b) gives the value of η_c. Equation 10c indicates the third and descending branch; λ_c is crushing energy constant as a material property. Utilizing the stress and strain compatibility at the strain level of $\varepsilon_c = 0.0035$, for Equation 10b and 10c enables the value of k_c to be determined. The ultimate strain (ε_u) of concrete was set to a large value of 0.035 to avoid any numerical setbacks. Table 1 indicates CDP parameters, used in the FEA software.

Table 1. CDP parameters [17].

Parameter	$\left(\sigma_{b0} / \sigma_{c0}\right)$	k_c	ψ	ζ	$\mu(s)$
Value	1.16	0.667	40°	0.1	0.00001

In this research, the linear uniaxial stress-strain behavior was used for concrete material. Concrete has a linear elastic behavior before reaching the peak tensile strength (in the first branch of modeling). Cracking and its propagation in concrete under tension happen in the second branch. The linear, bilinear, or nonlinear model used to model the softening procedure of concrete, is illustrated in Fig. 3. As regards to the computer configuration used to analyze the specimens, a computer system with a Core i7 CPU (central processing unit) with a capacity of 2.81 GHz (Gigahertz), an installed memory (RAM) 12 GB (Gigabyte), a hard disk drive with a capacity of 1000 GB, and a solid-state drive with a capacity of 128 GB was used.

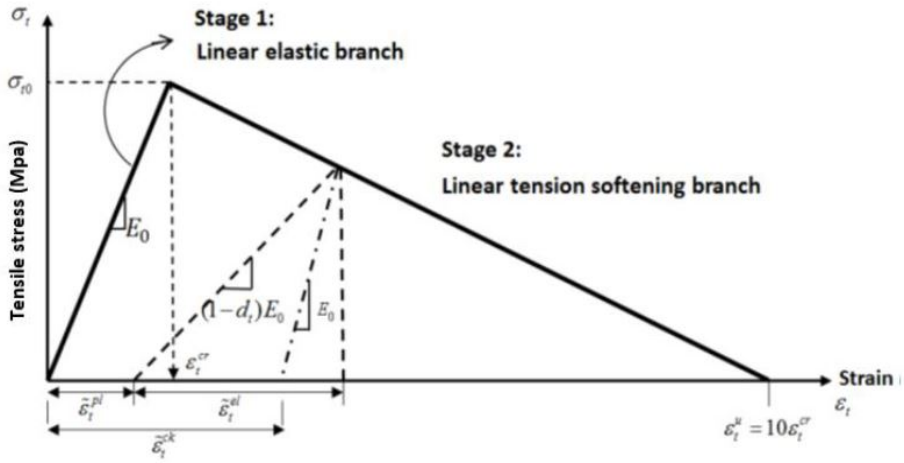

Figure 3. Uniaxial tensile stress-strain behavior of concrete with softening branch [18].

Equation 11 is used to evaluate the tensile strength of concrete:

$$f_t' = 0.33\sqrt{f_c'}. \tag{11}$$

2.2.2 Steel Reinforcement Modelling

The uniaxial tensile stress-strain behavior of bars was considered to be elastic with regard to conventional Young's modulus and Poisson's ratio. Also, the plastic behavior of steel was modeled. Bilinear behavior was used to define the properties of the plastic phase. Fig. 4 illustrates the typical stress-strain behavior of steel.

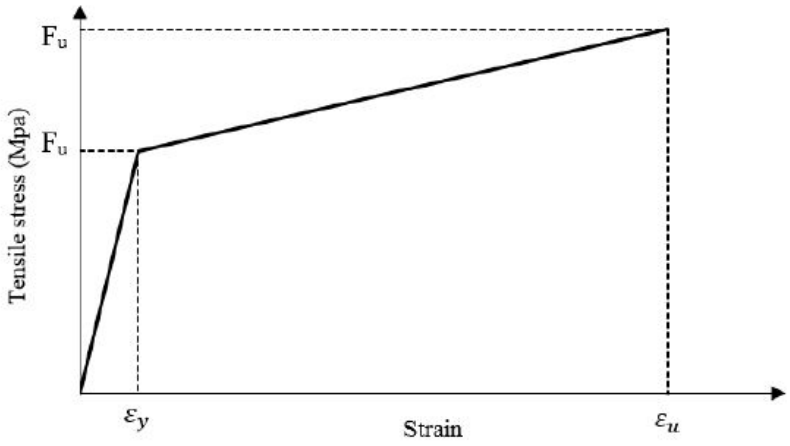

Figure 4. Uniaxial stress-strain behavior of steel [15].

2.2.3. Model Verification

The reliability of the analytical modeling to perform non-linear analysis on the numerical shear walls was investigated by verification of one shear wall based on the experimental studies of Oesterle *et al.* in 1979 [19]. The specifications of this specimen are shown in Tables 1 and 2. Fig. 5 and 6 also show the geometry of this specimen and the experimental setup. The geometry and steel bar layout of its boundary elements are demonstrated in Fig. 7. This specimen was analyzed under a unidirectional incremental lateral force. Applying the lateral load continued until failure of vertical moment bars of the boundary elements was observed. Moreover, this is the reference specimen and other specimens were designed based on it. In order to model a shear wall in the FEA software (ABAQUS), it had to be divided into seven different parts such as the shear wall, foundation, slab, longitudinal bar of the boundary elements, transverse bars of the boundary elements, vertical and the horizontal bars of the web. These parts were modeled separately and then assembled. The freedom degrees of both the top and bottom ends of the wall were fixed as shown in Fig. 8.

Table 2. Specifications of the material used in the reference specimen [19].

Model name	Shape	% (Reinforcement)				f_y (MPa)	$f_c^{'}$ (MPa)	Axial load (kN)
		ρ_s	ρ_n	ρ_h	ρ_f			
Reference specimen	With boundary elements	1.28	0.29	0.31	1.11	450	45	0

Table 3. Steel bars layout in the reference specimen [19].

Bar location	Bar layout	Considerations
Flexural bars of the boundary elements	8 #13	---
Horizontal bars of the web	#8 @330 mm	In two meshes
Vertical bars of the web	#8 @350 mm	In two meshes
Confinement bars	3#13 @60 mm	---

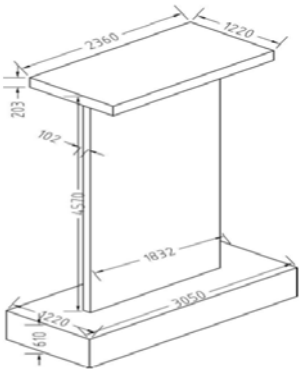

Figure 5. The geometry of the shear wall [19].

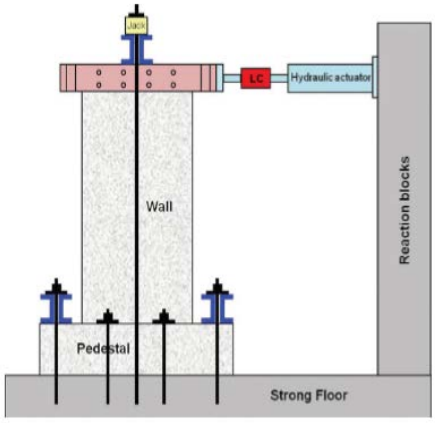

Figure 6. Experimental setup [19].

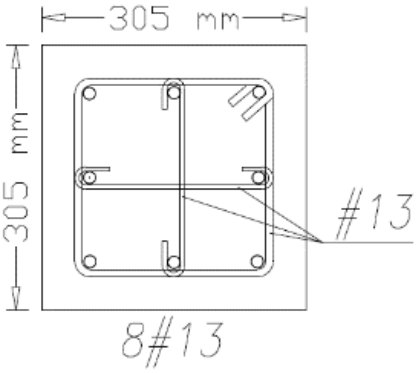

Figure 7. Specifications of the boundary elements.

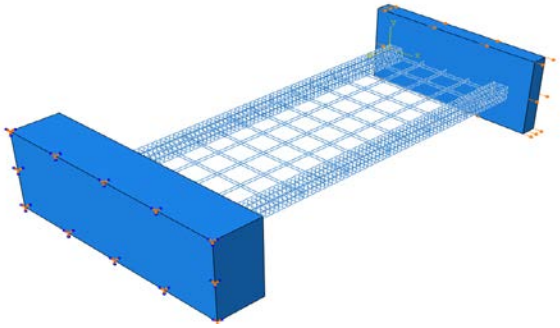

Figure 8. Modeling of steel bars and boundary condition.

Table 4 indicates the mechanical and analytical parameters used in the FEA software to model the reference specimen. The compressive strength of concrete in the reference specimen was 45 MPa, which its stress-strain diagram in tension and compression is shown in Fig. 9. In some of the specimens, concrete with compressive strengths of 30 or 60 MPa was used, which Fig. 10 and 11 show their stress-strain behavior.

Table 4. Mechanical and analytical parameters to model the 45 MPa concrete.

Name	$f_c^{'}$ (MPa)	n	E_c (MPa)	ε_0	ε_{cu}	K for $\varepsilon_c / \varepsilon_{c0} > 1$	$f_t^{'}$ (MPa)	ε_{cr}
Reference specimen	45	3.45	29,040	0.0022	0.008	1.396	3.7	1.28E-4

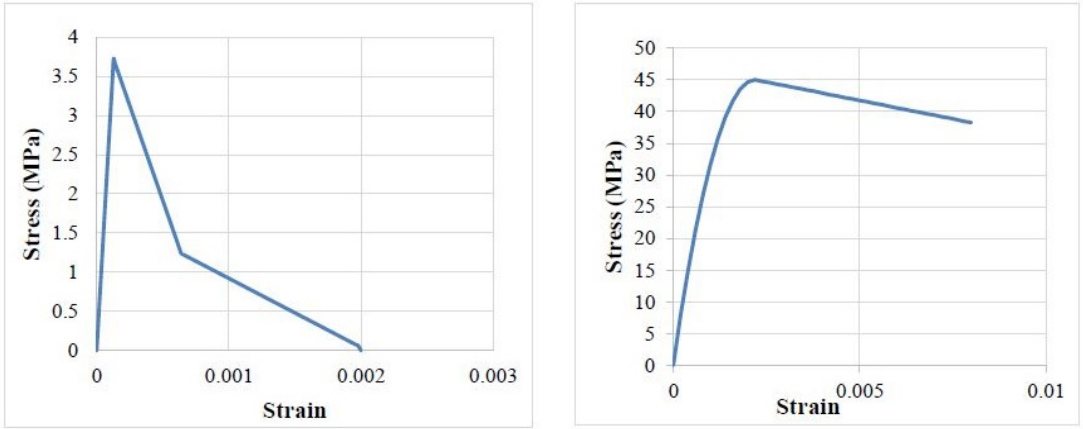

a b

Figure 9. Stress-strain diagram of 45 MPa concrete: a) tension and b) compression.

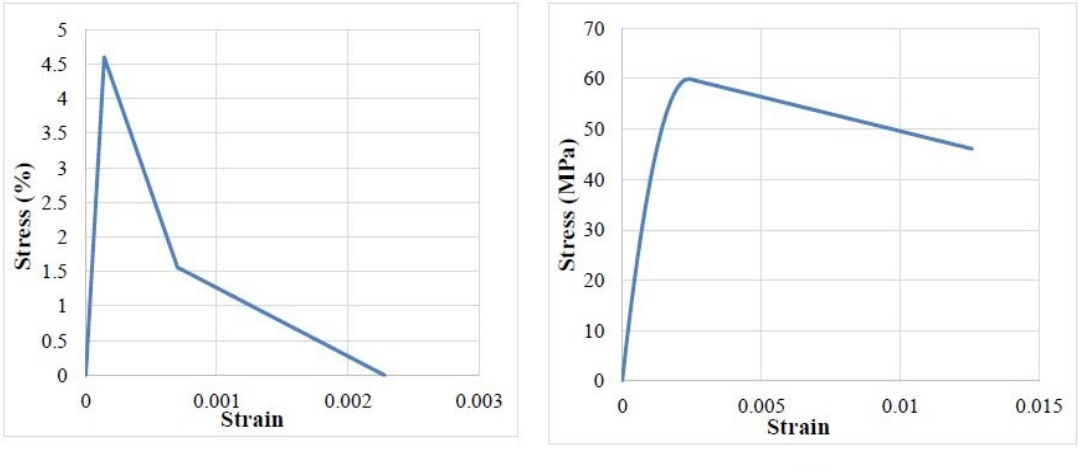

a b

Figure 10. Stress-strain diagram of 30 MPa concrete: a) tension and b) compression.

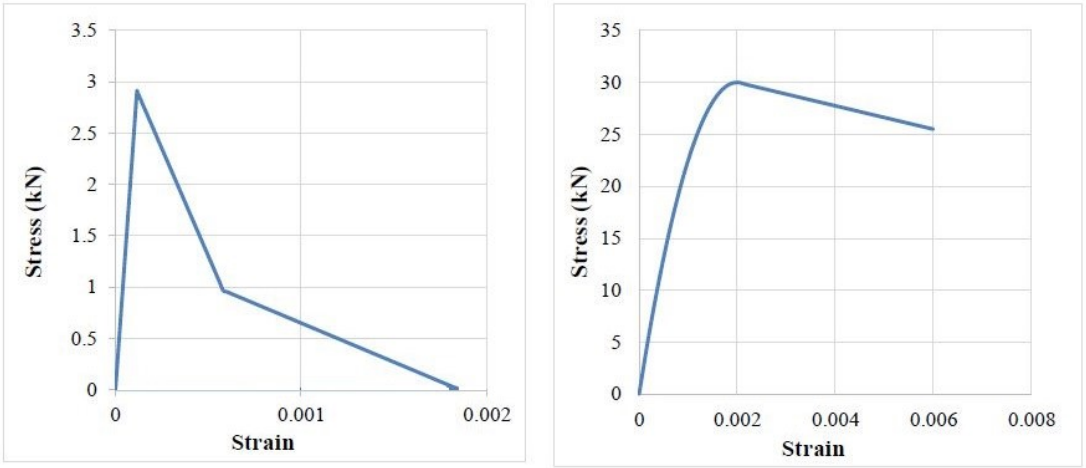

a b

Figure 11. Stress-strain diagram of 60 MPa concrete: a) tension and b) compression.

2.3. Mesh Configuration

Shear walls have plain stress behavior because of their small thickness in comparison to the other dimensions. There are three types of meshes such as fine, intermediate, and coarse ones. The more sensitive the structural parts, the finer the meshes. However, the results of the FEA software usually depend on the mesh sizes. This issue is a serious setback and its reason is modeling the cracks especially in the (SCC) modeling where the cracks propagate in the elements. There is effective mesh size in the non-linear FEA. This means that by using finer meshes, the more accurate results necessarily are not reached. This phenomenon is known as “mesh dependency”. Kheyroddin and Shayanfar (1997) proposed the below formulation for the effective mesh size in concrete (Equation 12) [20]:

$$\varepsilon_{tu} = 0.004e^{-0.008h}, \tag{12}$$

$h = \sqrt{A}$ and A is the area of the meshes, then h is their dimension. Then, with regard to the fact that $\varepsilon_{tu} = 0.002,$ the size of meshes in this study got 87 mm. Fig. 12 indicates the mesh configuration of specimens.

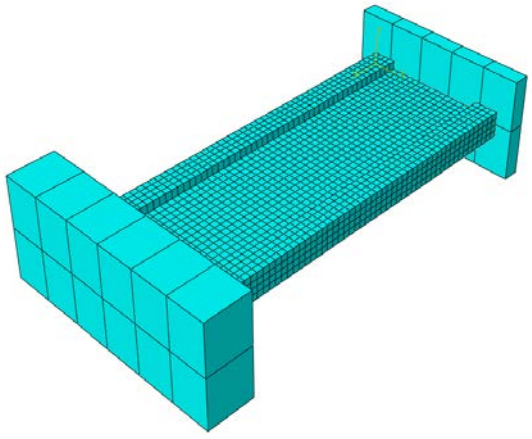

Figure 12. The meshing of the specimens.

2.4. Detail of Specimens

In this study, 45 shear walls were analyzed. With regard to the reference specimen, the first series of specimens were modeled by using concrete with the compressive strength of 45 MPa and steel bars with the yield strengths of 560 and 700 MPa as the vertical and horizontal bars of the web of specimens, and also as the flexural and shear bars of the boundary elements. Then, the other series of specimens were modeled by using concrete with the compressive strengths of 30 and 60 MPa along with the HSS bars.

The tantamount amounts of steel bars in the specimens were calculated by Equations 13 and 14 (based on the specifications of the bars in the reference specimen):

For the longitudinal bars:

$$N_1 A_{s1} f_{y1} = N_2 A_{s2} f_{y2}. \quad (13)$$

For the stirrups:

$$N_1 A_{sv1} f_{y1} \left(d_1/S_1\right) = N_2 A_{sv2} f_{y2} \left(d_2/S_2\right), \quad (14)$$

N is the number of bars, f_y is the yield strength of bars, A_s and A_{sy} are areas of longitudinal and transverse bars, d is effective depth of sections and S is the distance of stirrups**.** It must be noted that it is sufficient to put the number, yield strength, areas of bars of the base specimen in one side of the above equations, and the yield strength and areas of bars on the other side of the equation to find the equivalent number of the bars in the case of using the other types of bars. Indices 1 and 2 refer to the basic specimen and the specimen that was intended to find its equivalent number of the bars.

Table 6 shows the characteristics of the specimens. The specimens are named with respect to a rule, where the letter (C) stands for the concrete and the following number for its compressive strength in MPa. The letter (R) stands for reinforcement and the following number for one-tenth of yield strength of it in MPa. The final words stand for the location of HSS bars, for example, the word (all) stands for the case that HSS bars are used in all the bars, the word (bel) for the case of HSS bars as the flexural bars of the boundary elements, the word (s) for the case of using HSS bars as stirrups, the word (bels) for the flexural and shear bars of the boundary elements, the word (hw) for the case of using HSS bars as the horizontal bars of the web of the specimens, the word (vw) for the case of using HSS bars as the vertical bars of the web, and the word (hvw) for both the vertical and horizontal bars of the web.

Table 5. Specifications of the specimens.

Specimen	f_y (MPa)	f_c' (MPa)
C45R56all	**560**	**45**
C45R56bel	**560**	**45**
C45R56bels	**560**	**45**
C45R56s	**560**	**45**
C45R56hw	**560**	**45**
C45R56vw	**560**	**45**
C45R56hvw	**560**	**45**
C45R70all	**700**	**45**
C45R70bel	**700**	**45**
C45R70bels	**700**	**45**
C45R70s	**700**	**45**
C45R70hw	**700**	**45**
C45R70vw	**700**	**45**
C45R70hvw	**700**	**45**
C30R56all	**560**	**30**
C30R56bel	**560**	**30**
C30R56bels	**560**	**30**
C30R56s	**560**	**30**
C30R56hw	**560**	**30**
C30R56vw	**560**	**30**
C30R56hvw	**560**	**30**
C30R70all	**700**	**30**
C30R70bel	**700**	**30**
C30R70bels	**700**	**30**
C30R70s	**700**	**30**
C30R70hw	**700**	**30**
C30R70vw	**700**	**30**
C30R70hvw	**700**	**30**
C60R56all	**560**	**60**
C60R56bel	**560**	**60**

Specimen	f_y (MPa)	f_c' (MPa)
C60R56bels	**560**	**60**
C60R56s	**560**	**60**
C60R56hw	**560**	**60**
C60R56vw	**560**	**60**
C60R56hvw	**560**	**60**
C60R70all	**700**	**60**
C60R70bel	**700**	**60**
C60R70bels	**700**	**60**
C60R70s	**700**	**60**
C60R70hw	**700**	**60**
C60R70vw	**700**	**60**
C60R70hvw	**700**	**60**
C45R42	**420**	**45**
C60R42	**420**	**60**
C30R42	**420**	**30**

3. Results and Discussion

3.1. Load-Displacement Diagrams

One of the important results of the FEA is the diagram of load (shear force) – displacement. There are paramount parameters that can be deducted from this diagram such as the loading capacity, ductility, and energy absorption. Fig. 13 indicates the comparison of the load-displacement diagram of the specimens which have the concrete with compressive strength of 45 MPa and HSS bars with a yield strength of 700 MPa. The results showed that using 700 MPa bars as the different bar types of specimens led to an increase in their loading capacity. The WC45R70all specimen which had 700 MPa steel as all of its bars, had the greatest loading capacity in comparison to the other specimens. This loading-capacity increase was nearly 57 % in comparison to the reference specimen.

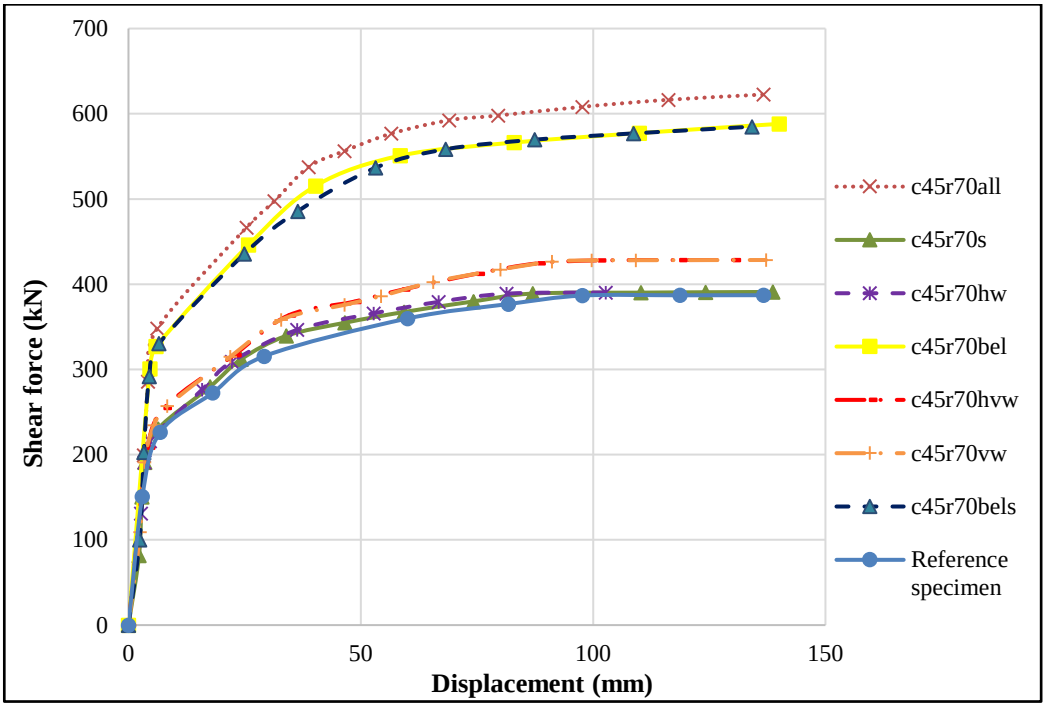

Figure 13. Load-displacement diagram of the specimens with 700 MPa HSS bars.

Fig. 14 demonstrates the effect of using different types of concrete along with HSS bars on the load-displacement diagram. The results showed that using different types of concrete did not have a considerable effect on the behavior of specimens. These results were in accordance with the experimental observations of Arshadi et al. in their experiments on the HSS effects on the load-displacement diagrams of RC members [2, 11].

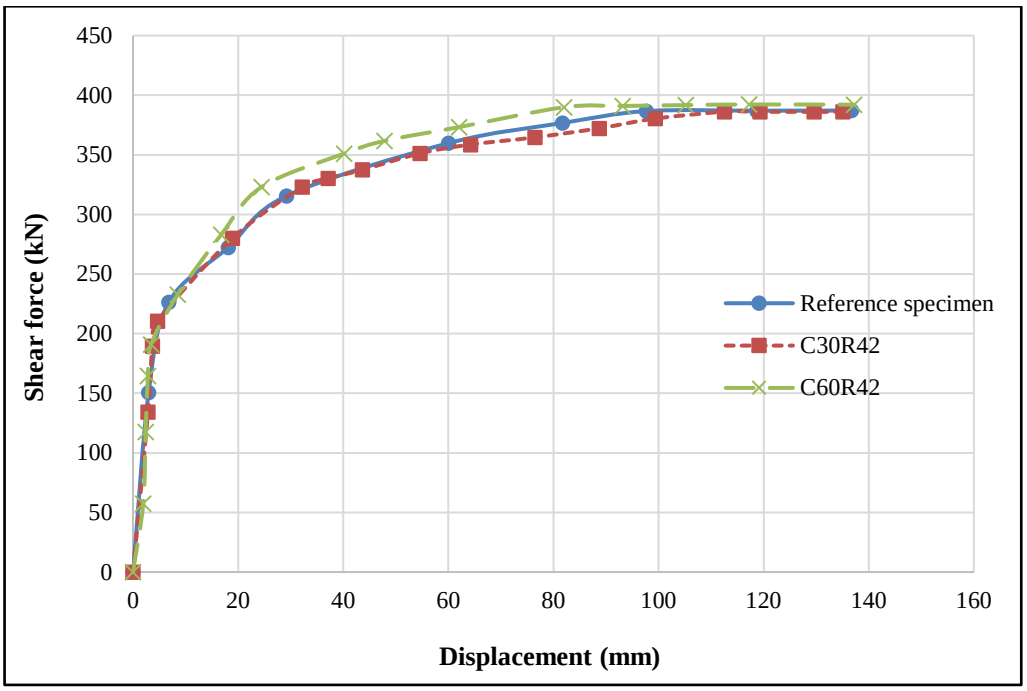

Figure. 14. Load-displacement diagram of the specimens with different concrete types.

3.2. Base Shear

Fig. 15 indicates the effect of using HSS bars and different types of concrete along with each other. Generally, it was observed that using higher-strength concrete along with HSS bars led to increasing the maximum base shear of the specimens. However, the differences between the maximum base shear of specimens with different concrete types were not considerable. These differences were rather negligible in the cases of using HSS bars as the flexural and shear bars of the boundary elements (bels) and as the flexural bars of the boundary elements (bel). On the other hand, the effects of applying HSS bars in different cases were considerable. It was also observed that the higher the steel strength, the greater the maximum base shear. It must be mentioned that in the cases of using HSS bars as the horizontal bars of the web of the specimens (hw) and as the stirrups, the diagrams approximately became horizontal. This means that the effects of using higher-strength bars in these cases were not considerable. These results and patterns were similar to those of Kolozvary and Wallace (2016) and Arshadi *et al.* (2019) [8, 10].

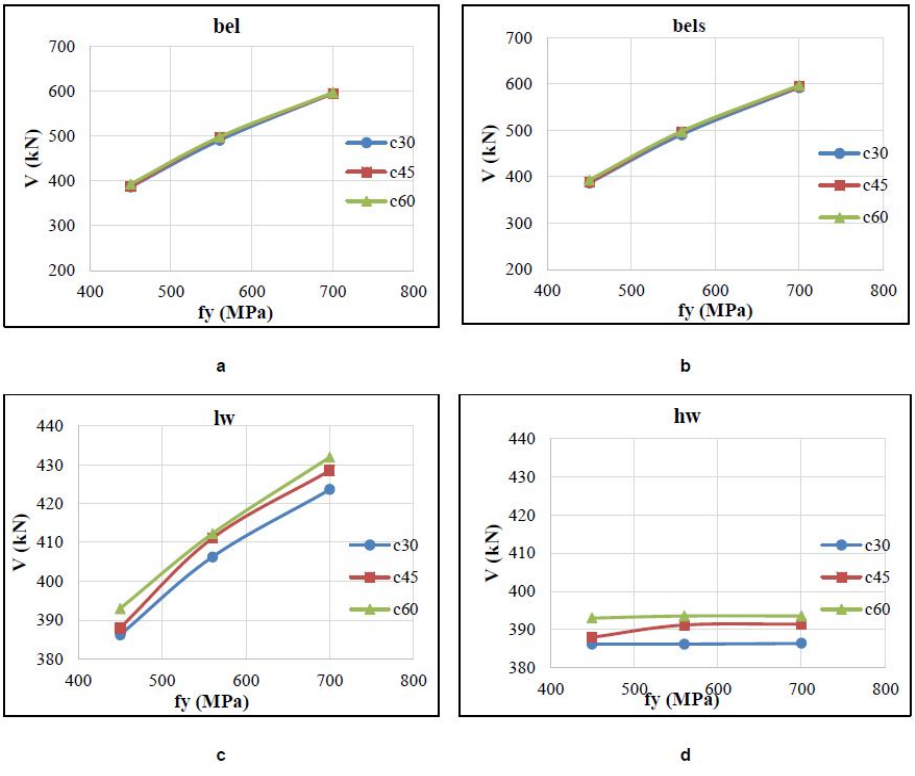

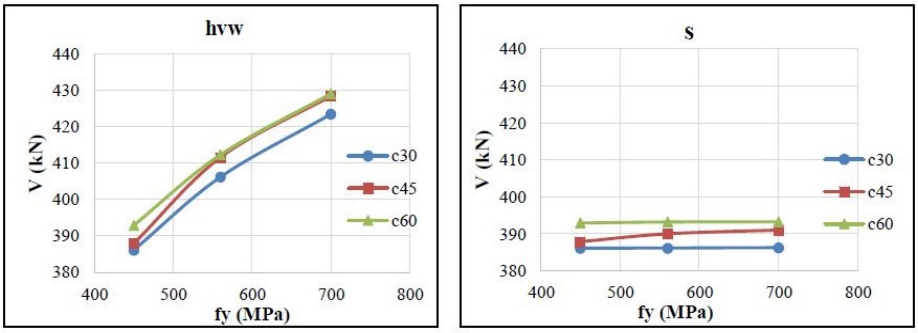

e f

Figure 15. Effects of HSS bars and different concrete types on the maximum base shear in different cases of: a) bel, b) bels, c) lw, d) hw, e) hvw, and f) s.

Fig. 16 and 17 indicate the comparison of maximum base shears in different cases of using HSS bars in the specimens. In order to prevent more complications and make the figures simpler, numbers from 1 to 6 are assigned to the different cases of using HSS bars, as shown in Table 6. The results showed that the C60R70all and C45R70all had the greatest maximum base shears among the specimens. Moreover, the C30R56s, C30R56hw, C30R56s, and C30R56hw had the least maximum base shears among the specimens. The results also showed that using lower-strength bars (such as bars with the f_y of 300 and 560 MPa) had fewer effects on the maximum base shear than using 700 MPa steel.

Table 6. Numbering different cases of the reinforcement layout.

Notation	Number
s	1
hw	2
vw	3
hvw	4
bel	5
bels	6
all	7

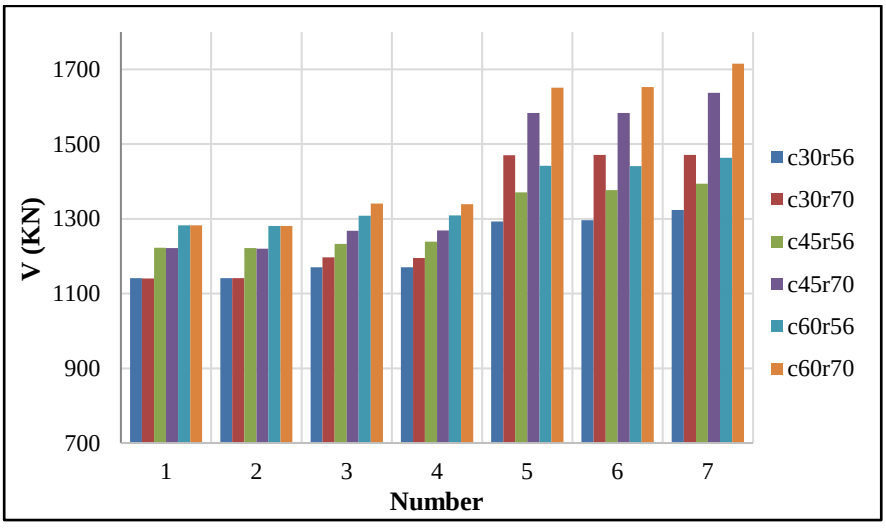

Figure. 16. Comparison of the maximum base shears.

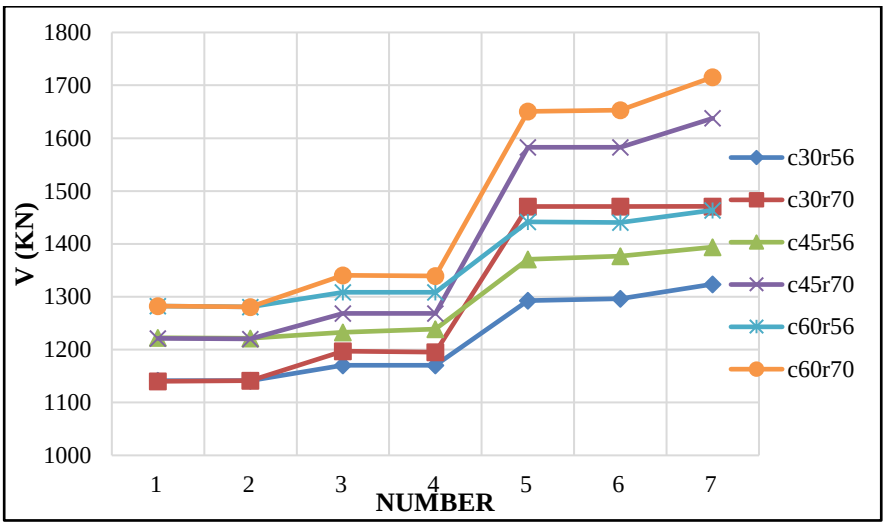

Figure 17. Comparative diagrams of the maximum base shears.

The results generally demonstrated that HSS usage as flexural bars of boundary elements improved the performance of specimens in terms of the maximum base shear more than the other cases of the bar locations. However, their application as shear reinforcement of the boundary elements did not affect their performance, significantly. Besides, HSS application as the horizontal and vertical bars improved the performance of specimens. It must be mentioned that using HSC and HSS bars also improved the behavior of specimens and C60R70 had the best behavior among the specimens.

3.3. Ultimate Moment

Fig. 18 indicates the effect of using HSS bars and different types of concrete along with each other in different locations of HSS bars on the ultimate moment of the specimens. The results demonstrated that applying higher-strength concrete along with HSS bars ended up increasing the ultimate moment of the specimens. Unlike the maximum base shear force, the differences between the ultimate moments of the specimens with different concrete types were not negligible. Besides, the influences of using HSS bars in discrepant cases were conspicuous. Like the maximum base shear, the higher the strength of the steel, the greater the ultimate moment. The diagrams got approximately horizontal by applying HSS bars as the horizontal and vertical bars of the web of the specimens (hvw), as the horizontal bars of the web of the specimens (hw), as the vertical bars of the web of the specimens, and as the stirrups. This means that the effects of using higher-steel bars in these cases were not considerable.

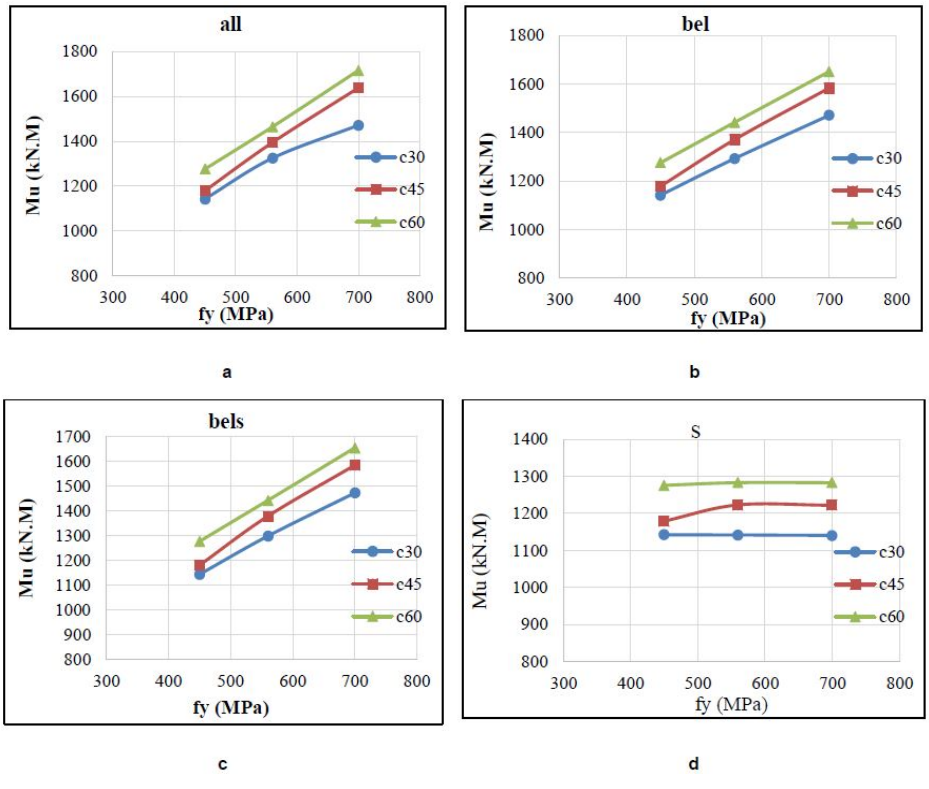

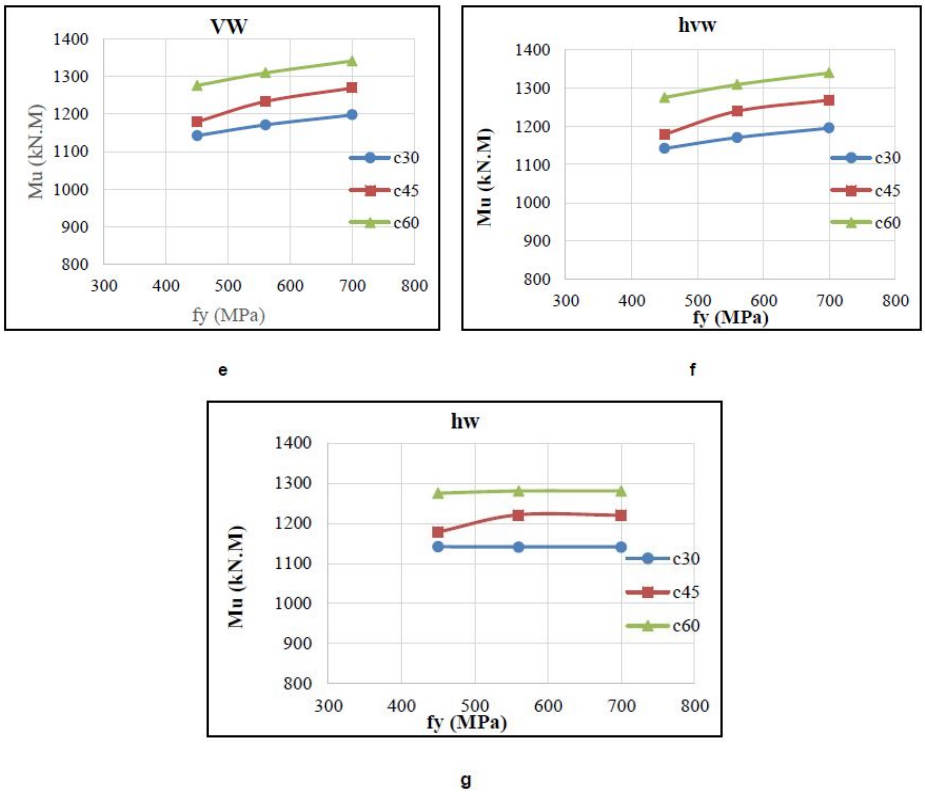

Figure 18. Effects of HSS bars and concrete types on the ultimate moments in different cases of: a) all, b) bel, c) bels, d) s, e) vw, f) hvw, and g) hw.

Fig. 19 and 20 demonstrate the analogy between the ultimate moment values in different cases of applying HSS bars in the specimens. As for the ultimate moment a rather similar process was observed, too. The results indicated that the C60R70all and C45R70all specimens had the greatest ultimate moment among the specimens. The C30R56s, C30R56hw, C30R56s, and C30R56hw specimens had the least ultimate moment among the specimens. Besides, using lower-grade steel bars (such as steel bars with the f_y of 300 and 560 MPa) had fewer influences on the ultimate moment than using 700 MPa steel. At last, the results demonstrated that using higher-strength steel was more effective on the shear base values of the specimens than their ultimate moment values. These results were in accordance with those of previous studies such as the studies of Kolozvary *et al.* (2018) and Tanyeri *et al.* (2014) [9, 19].

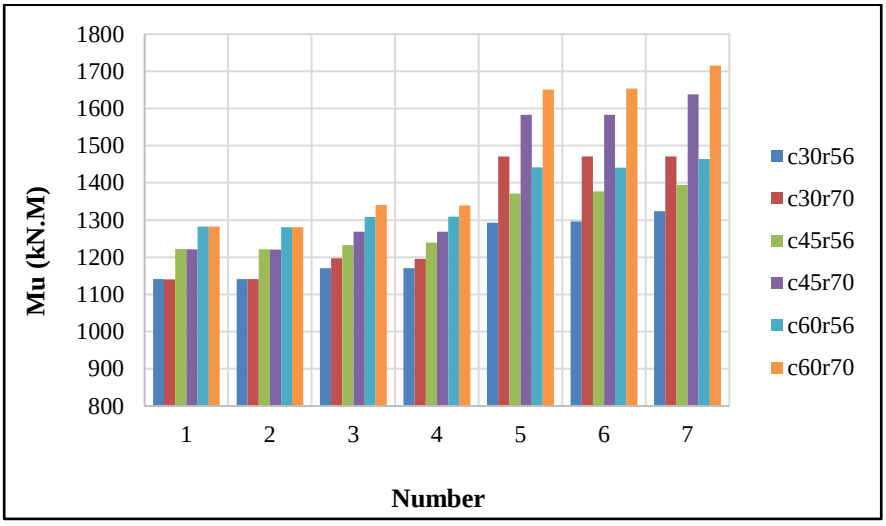

Figure 19. Comparison of the ultimate moments of the specimens.

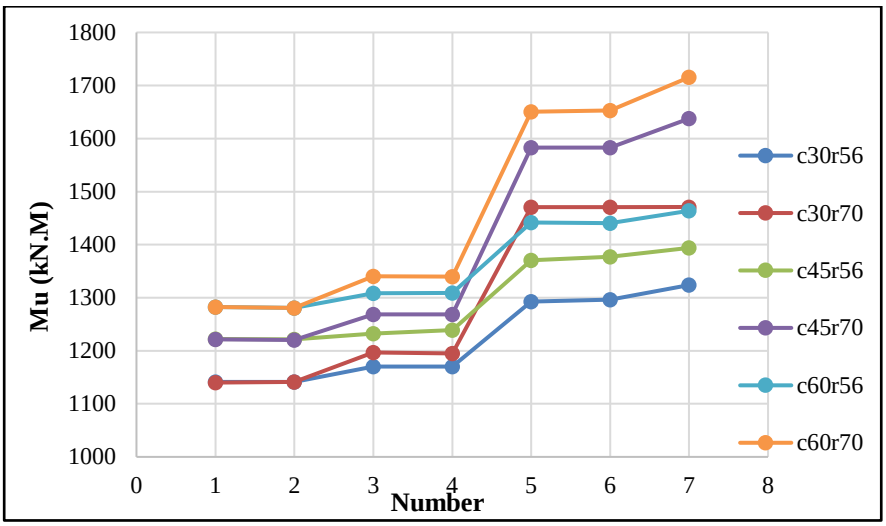

Figure 20. Comparative diagrams of the ultimate moments of the specimens.

As for the ultimate moment, a similar method to the maximum base shear is observed, too. The results generally indicated that HSS usage as flexural bars of boundary elements improved the performance of shear walls (in terms of the ultimate moment) more than the other cases of bar locations. However, their application as the shear bars of the boundary elements did not affect their performance, considerably. Besides, HSS application as the horizontal and vertical bars improved the performance of specimens. Also, using higher-strength concrete was less effective than using higher-strength steel on the maximum base shear and the ultimate moment of the specimens. Finally, the application of both HSC and HSS bars together improved the behavior of specimens. The C60R70 had the best behavior among the specimens.

Table 7 indicates the maximum base shear and ultimate moment variation percentages of the specimens in comparison to those of the reference specimen. As for the maximum base shear, the C30R70all specimen had the greatest maximum base shear variation percentage (69 %) and the C30R42 had the least percentage (–0.5 %) among the specimens. Moreover, as for the ultimate moment, the C60R70all had the greatest ultimate moment variation percentage (45 %) and the C30R42 had the least percentage (–3.1 %).

Table 7. Variation percentages of the maximum base shear and the ultimate moment of the specimens.

Specimen	ΔM_U (%)	ΔV(%)
C45R56all	**18**	**33**
C45R56bel	**16**	**28**
C45R56bels	**17**	**28**
C45R56s	**4**	**1.4**
C45R56hw	**4**	**1.4**
C45R56vw	**6**	**5.9**
C45R56hvw	**6**	**6**
C45R70all	**39**	**63**
C45R70bel	**34**	**53**
C45R70bels	**34**	**53**
C45R70s	**4**	**1.4**
C45R70hw	**4**	**1.4**
C45R70vw	**8**	**6.4**
C45R70hvw	**9**	**10.4**
C30R56all	**13**	**32**
C30R56bel	**9.7**	**26**
C30R56bels	**10**	**26**
C30R56s	**–3**	**–0.46**
C30R56hw	**–3**	**–0.46**
C30R56vw	**–1**	**4.7**
C30R56hvw	**–1**	**4.7**

Specimen	ΔM_U (%)	ΔV(%)
C30R70all	**26**	**69**
C30R70bel	**25**	**53**
C30R70bels	**26**	**53**
C30R70s	**–3**	**–0.4**
C30R70hw	**–3**	**–0.4**
C30R70vw	**–1**	**6.4**
C30R70hvw	–1	**6.4**
C60R56all	**24**	**46**
C60R56bel	**22**	**28**
C60R56bels	**23**	**28**
C60R56s	**9**	**1**
C60R56hw	**9**	**1.4**
C60R56vw	**11**	**6.2**
C60R56hvw	**11**	**6.3**
C60R70all	**45**	**63**
C60R70bel	**40**	**53**
C60R70bels	**41**	**54**
C60R70s	**9**	**1.43**
C60R70hw	**9**	**1.4**
C60R70vw	**14**	**6.4**
C60R70hvw	**14**	**6.5**
C45R42	**0**	**0**
C60R42	**8**	**1.3**
C30R42	**–3.1**	**–0.5**

4. Conclusion

Scientific developments facilitated producing HSS bars with suitable engineering characteristics such as appropriate ductility along with high strength. Despite several economical and executive profits of HSS bars, their application is limited in special shear walls and moment frames, because of possible repercussions related to their possible effects on decrease in ductility, energy absorption, and so forth. A lack of experimental and analytical data about the seismic behavior of shear walls with HSS bars can be the source of this problem. In this research, the influences of using HSS bars with the yield strengths of 560 and 700 MPa as horizontal and vertical bars of the web, and as the flexural and shear bars of the boundary elements on the behavior of shear walls, were analytically investigated by FEA. The effects of concrete strength (with the compressive strengths of 30, 45, and 60 MPa) in the case of using HSS bars in the shear walls were investigated, too. The results indicated that HSS application as flexural bars of boundary elements improved the performance of the specimens significantly. However, their application as the shear bars of the boundary elements did not considerably affect their performance. Moreover, HSS application as the horizontal and vertical bars of the web of specimens improved their performance. It was also observed that using higher-strength concrete was less effective than using higher-strength steel on the maximum base shear and the ultimate moment of the specimens. Finally, the results showed that using higher-strength steel was more effective in the shear performance of specimens than their ultimate moment.

References

1. Arshadi, H., Kheyroddin, A. Shear lag phenomenon in the tubular systems with outriggers and belt trusses. Magazine of Civil Engineering. 2019. 86(2). Pp. 105–118. DOI: 10.18720/MCE.86.10
2. Siddika, A., Mamun, M.A., Al, Alyousef, R., Amran, Y.H.M. Strengthening of reinforced concrete beams by using fiber-reinforced polymer composites: A review. 25. Elsevier Ltd, 2019.
3. Arshadi, H., Kheyroddin, A., Naderpour, H. An investigation into the behavior of special moment frames with high-strength reinforcement subjected to cyclic loading. Journal of Building Engineering. 2019. DOI: 10.1016/j.jobe.2019.100905
4. Kelly, D.J., Lepage, A., Mar, D., Restrepo, J.I., Sanders, J.C., Taylor, A.W. Use of high-strength reinforcement for earthquake-resistant concrete structures. NCEE 2014 – 10th U.S. National Conference on Earthquake Engineering: Frontiers of Earthquake Engineering. 2014. DOI: 10.4231/D3Z31NP6Z
5. Aoyama, H. Design of modern highrise reinforced concrete structures 2001.
6. Zhou, J., Chen, S., Chen, Y. Calculation methods of the crack width and deformation for concrete beams with high-strength steel bars. Frontiers of Structural and Civil Engineering. 2013. DOI: 10.1007/s11709-013-0211-0
7. Kolozvari, K., Wallace, J.W. Practical Nonlinear Modeling of Reinforced Concrete Structural Walls. Journal of Structural Engineering (United States). 2016. DOI: 10.1061/(ASCE)ST.1943-541X.0001492

8. Kheyroddin, A., Arshadi, H., Binaipur, F. An Overview of the Effects of High-Strength Reinforcement (HSR) on the Intermediate Moment-Resisting Frames. 2017. 1(2). Pp. 177–187. DOI: 10.22060/ceej.2017.12406.5207
9. Kolozvari, K., Orakcal, K., Wallace, J.W. New opensees models for simulating nonlinear flexural and coupled shear-flexural behavior of RC walls and columns. Computers and Structures. 2018. DOI: 10.1016/j.compstruc.2017.10.010
10. Arshadi, H., Kheyroddin, A., Naderpour, H. High-strength reinforcement effects on the seismic behaviour of beam–column joints. Proceedings of the Institution of Civil Engineers – Structures and Buildings. 2019. DOI: 10.1680/jstbu.18.00225.
11. Alaee, P., Li, B. High-strength concrete exterior beam-column joints with high-yield strength steel reinforcements. Engineering Structures. 2017. 145. Pp. 305–321. DOI: 10.1016/j.engstruct.2017.05.024
12. Sadraie, H., Khaloo, A., Soltani, H. Dynamic performance of concrete slabs reinforced with steel and GFRP bars under impact loading. Engineering Structures. 2019. 191(December 2018). Pp. 62–81. DOI: 10.1016/j.engstruct.2019.04.038.
13. Feng, D.C., Ren, X.D., Li, J. Cyclic behavior modeling of reinforced concrete shear walls based on softened damage-plasticity model. Engineering Structures. 2018. 166(November). Pp. 363–375. DOI: 10.1016/j.engstruct.2018.03.085
14. Hafezolghorani, M., Hejazi, F., Vaghei, R., Jaafar, M.S. Bin, Karimzade, K. Simplified damage plasticity model for concrete. Structural Engineering International: Journal of the International Association for Bridge and Structural Engineering (IABSE). 2017. 27(1). Pp. 68–78. DOI: 10.2749/101686616X1081
15. Liao, F.Y., Han, L.H., Tao, Z. Performance of reinforced concrete shear walls with steel reinforced concrete boundary columns. Engineering Structures. 2012. DOI: 10.1016/j.engstruct.2012.05.037
16. Khani, J., Bozorg, M., Zahrai, S.M. Investigating Seismic Behavior of Reinforced Concrete Columns with SFRP Using Finite Element Method. American Journal of Engineering and Applied Sciences. 2018. 11(2). Pp. 996–1004. DOI: 10.3844/ajeassp.2018.996.1004
17. Mo, Y.L., Zhong, J., Hsu, T.T.C. Seismic simulation of RC wall-type structures. Engineering Structures. 2008. DOI: 10.1016/j.engstruct.2008.04.033
18. Tanyeri, A.C., Moehle, J.P., Nagae, T. Seismic performance and modeling of post-tensioned, precast concrete shear walls. NCEE 2014 – 10th U.S. National Conference on Earthquake Engineering: Frontiers of Earthquake Engineering. 2014. DOI: 10.4231/D34M91B3B
19. Colotti, V. Shear behavior of RC structural walls. Journal of Structural Engineering (United States). 1993. DOI: 10.1061/(ASCE)0733-9445(1993)119:3(728)
20. Colotti, V. Shear behavior of RC structural walls. Journal of Structural Engineering (United States). 1993. DOI: 10.1061/(ASCE)0733-9445(1993)119:3(728)

Information about authors:

***Hamed Arshadi**, PhD,*

ORCID: https://orcid.org/0000-0002-3305-1782

E-mail: hamed.arshadi@semnan.ac.ir

***Ali Kheyroddin**, PhD,*

ORCID: https://orcid.org/0000-0001-7802-2013

E-mail: kheyroddin@semnan.ac.ir

Amir Asadollahi Nezhad,

E-mail: hamed.arshadi@yahoo.com

Received 05.07.2020. Approved after reviewing 12.07.2021. Accepted 13.07.2021.